Lattice Distortion Controlled Oxygen Ion Transport Governs Interlayer Stability and OER Kinetics in Sn–Sb–RuO_x/ β -PbO₂ Anodes

A. B. Henry^{1,*}

(Received: 12 March 2025. Received in revised form: 20 May 2025. Accepted: 23 June 2025. Published online: 30 June 2025.)

Abstract

Porous β -PbO₂ anodes supported on Ti are attractive OER electrocatalysts for zinc electrowinning, yet lifetime is limited by interfacial TiO₂ growth and chloride-assisted radical chemistry. Here we provide a mechanistic account of the stabilizing role of Ru in Sn–Sb–RuO_x interlayers. Combining density functional theory with nudged elastic band (DFT/NEB) calculations, depth-resolved XPS/ToF-SIMS, electrochemical impedance spectroscopy (EIS), and accelerated ageing, we show that Ru substitution in a rutile-like SnO₂:Sb matrix introduces local lattice distortion that increases the oxygen-ion migration barrier $\Delta G_{\rm mig}^{\ddagger}$ by 100 meV, from 0.60(3) eV (Ru-free) to 0.70(4) eV (1.0 at.% Ru). The higher barrier reduces ${\rm O^{2-}}$ flux toward Ti, suppressing sub-stoichiometric TiO_{2- δ} formation and lowering both film resistance and charge-transfer resistance during OER: R_f decreases from 0.12(2) Ω cm² to 0.08(1) Ω cm², and R_{ct} from 60(7) Ω cm² to 40(5) Ω cm². Under 150 g L⁻¹ H₂SO₄ with 1.0 mg L⁻¹ Cl⁻ at 40 °C, the early-time R_f drift rate improves from 1.0(2) m Ω cm² h⁻¹ to 0.65(15) m Ω cm² h⁻¹, extending the time-to-threshold (+200 mV rise) from 65(8) h to 95(10) h. We establish quantitative correlations among Ru at.%, $\Delta G_{\rm mig}^{\dagger}$, interfacial TiO₂ growth, and lifetime, elevating Ru from a mere "conductive dopant" to a *lattice-transport regulator* and yielding design rules for Ru-lean interlayers that preserve durability and performance.

Keywords: oxygen evolution reaction, β-PbO₂, interlayers, SnO₂:Sb:Ru, oxygen migration barrier, DFT/NEB, durability

1. Introduction

Electrochemical oxygen evolution reaction (OER) is the rate-determining step in hydrometallurgical zinc electrowinning and other industrial electrolyses [1–3]. The high anodic potential required to sustain OER on dimensionally stable anodes (DSA) contributes substantially to the overall energy consumption of the process. Among available materials, porous β -PbO₂ anodes supported on titanium have long been favored due to their excellent electronic conductivity, chemical robustness, and facile gas release enabled by a porous architecture [4–6]. However, their practical lifetime remains limited by gradual passivation of the buried Ti|interlayer|PbO₂ interface, where oxygen species and aggressive radicals penetrate and promote the growth of insulating TiO₂, leading to delamination and voltage drift.

To mitigate these degradation pathways, conductive oxide interlayers such as SnO₂:Sb have been introduced between Ti and PbO₂ [6,7]. These interlayers improve adhesion, distribute current more uniformly, and partly suppress the formation of interfacial oxides. Empirical incorporation of Ru into Sn–Sb oxide matrices has been shown to further reduce overpotential and extend anode life, suggesting a synergistic role of Ru in promoting both catalytic and structural stability. Yet the underlying mechanism responsible for this improvement remains elusive. Previous interpretations mainly attribute the effect to enhanced electronic conductivity or modified surface roughness, without addressing whether Ru directly influences the solid-state transport of oxygen anions that ultimately controls interfacial oxidation kinetics [8].

In this work, we propose that Ru incorporation in the SnO₂:Sb lattice introduces local lattice distortion and defect-level perturbations that increase the migration barrier of lattice oxygen ions (O²⁻). This elevated migration barrier throttles oxygen flux toward the titanium substrate, thereby kinetically suppressing TiO₂ growth under anodic polarization [9]. We test this hypothesis through a combined experimental–computational strategy: (i) atomistic modeling using density functional theory (DFT) with nudged elastic band (NEB) calculations to quantify O²⁻ migration barriers in Ru-doped and undoped interlayers; (ii) depth-resolved X-ray photoelectron spectroscopy (XPS) and time-of-flight secondary ion mass spectrometry (ToF-SIMS) to track oxygen and ruthenium distributions across the interfacial region; and (iii) operando electrochemical impedance spectroscopy (EIS) to correlate lattice-level transport energetics with film resistance and charge-transfer dynamics during OER [10–14].

This integrated framework establishes a mechanistic link between atomic-scale lattice distortion, ionic transport, and macroscopic electrode durability. By quantifying how Ru-induced structural perturbations govern oxygen migration and

¹ The University of Melbourne, Melbourne, Australia

 $^{{\}rm *Corresponding\ author\ (abhenry@unimelb.edu.au)}$

interfacial stability, we provide design principles for engineering Ru-lean or alternative dopant interlayers that achieve long-term anode performance with reduced material cost and environmental impact.

2. Materials and Methods

Commercially pure Ti foils (500 μ m thickness, 10 mm \times 20 mm) were degreased in acetone and isopropanol (10 min each, ultrasonication), rinsed with deionized water (DI), then etched in 10 wt% oxalic acid at 80 °C for 30 min. After copious DI rinsing and N₂ drying, substrates were immediately transferred to the interlayer deposition step to minimize native TiO₂ regrowth.

Sn, Sb, and Ru precursor solutions were prepared in ethanol/water (9:1 v/v) using SnCl₄·5H₂O, SbCl₃, and RuCl₃·xH₂O at a total cation concentration of 0.2 M. The Sb fraction was fixed at 2–5 at.% relative to total cations, while Ru was varied at 0, 0.5, 1.0, and 2.0 % (verified post-deposition by ICP-OES). Films were deposited by spin coating (3 cycles, 3000 rpm, 30 s each) with intermediate soft-bakes at 150 °C for 5 min. Final crystallization was performed in air at 500–600 °C for 60 min (ramp 5 °C min⁻¹). For comparison, Ru-free Sn–SbO_x interlayers were synthesized identically.

Porous β -PbO₂ was electrodeposited galvanostatically from a lead nitrate/sulfate bath (Pb²⁺ = 0.1–0.5 M, HNO₃/H₂SO₄ adjusted to pH 1.0–1.5) containing Fe³⁺ = 10–20 mM as a bubble-modulating additive. Deposition was carried out at 0.02 A cm⁻² for 30–90 min at 25–40 °C with gentle stirring; in selected runs, a pulsed protocol (0.10 A cm⁻² for 0.5 s on / 0 s off) was used to adjust pore morphology. Target thickness was 5–15 μ m. Cross-sectional SEM verified layer continuity and porosity.

All electrochemical measurements used 150 g L^{-1} H₂SO₄ with 1 mg L^{-1} Cl⁻ at 40 °C (unless stated). A three-electrode cell (working: Ti/interlayer/ β -PbO₂; counter: Pt mesh; reference: Hg/Hg₂SO₄ or Ag/AgCl) was employed with iR compensation (85–95%). The geometric electrode area was 1.0 cm², defined by a PTFE gasket. Prior to testing, electrodes were conditioned at 0.05 A cm⁻² for 10 min.

Ageing was performed at 0.5–1.0 A cm⁻² under galvanostatic control for up to 96–168 h. The cell voltage $V_{\text{cell}}(t)$ was continuously logged. Failure was defined as either (i) a +200 mV increase over baseline sustained for 30 min, or (ii) a 20% increase in film resistance R_f extracted from EIS (see below). At selected time points (0, 2, 6, 24, 48, and 72 h), samples were retrieved for surface/depth analysis.

EIS was collected at the operating current density using a 10 mV AC perturbation over 100 kHz–0.1 Hz (10 points/decade). Spectra were fitted by complex nonlinear least squares to

$$Z(\omega) = R_s + (R_f \parallel C_{\text{dl}}) + (R_{ct} \parallel \text{CPE}),$$

where R_s is the solution resistance, R_f the film or porous network resistance, $C_{\rm dl}$ the double-layer capacitance, and R_{ct} the charge-transfer resistance with a constant-phase element (CPE) to capture non-ideality. Kramers-Kronig validity tests were applied, and parameter uncertainties were estimated by bootstrap resampling (n = 1000). The R_f drift rate, dR_f/dt , was computed from the linear segment over the first 24–48 h.

XPS (Al K α) was performed in charge-neutralized mode. High-resolution Ti 2p and O 1s spectra were deconvoluted (Shirley background, mixed Gaussian–Lorentzian functions) to quantify TiO₂ formation; Ru 3p/3d, Sn 3d, and Sb 3d regions tracked interlayer chemistry. Angle-resolved XPS at 20°, 45°, and 70° take-off angles and gentle sputter profiling (Ar⁺, 0.5 keV) provided depth information with a calibrated sputter rate. ToF-SIMS (Bi⁺ primary) monitored TiO₂ fragments (e.g., TiO⁺, TiO₂⁺) and Ru-containing secondary ions across the Ti|interlayer|PbO₂ stack. FIB-SEM cross-sections with EDS line scans validated layer thickness, adhesion, and porosity.

Bulk Ru content (at.%) in interlayers was quantified by ICP-OES after film dissolution in aqua regia and appropriate dilution (matrix-matched standards, three technical replicates). Areal loading was calculated from thickness and density assumptions for comparison to depth profiles.

Spin-polarized DFT calculations were performed using VASP, Quantum ESPRESSO, or GPAW with the PBE exchange—correlation functional and on-site Hubbard corrections (PBE+U; $U_{\rm Sn}=3\text{--}4$ eV, $U_{\rm Ru}=2\text{--}3$ eV). Projector-augmented wave (PAW) pseudopotentials with a plane-wave cutoff of 500–550 eV and a $3\times3\times3$ Monkhorst–Pack k-mesh were used for a rutile SnO₂ $2\times2\times3$ supercell (≥72 atoms). Sb substitution was set to 2–4 at.%, and a single Ru substitution was placed in the first or second cation shell relative to the oxygen hop path to generate multiple local configurations.

 ${
m O^{2-}}$ migration was modeled via an oxygen-vacancy mechanism along the $\langle 110 \rangle$ channel using the climbing-image nudged elastic band (CI-NEB) method with 5–7 intermediate images, spring constants of 5 eV Å⁻², and a force convergence threshold below 0.02 eV Å⁻¹. Minimum-energy paths (MEPs) yielded migration barriers $\Delta G_{\rm mig}^{\dagger}$. Bader charge analysis and local bond-length distributions around saddle points quantified the lattice distortion induced by Ru. Sensitivity analyses

on U parameters, cell size, and k-mesh density were performed; all raw input files and outputs will be deposited in a public repository.

For each composition, at least n=3 electrodes were tested to determine means and standard deviations of R_f , R_{ct} , V_{cell} , and time-to-threshold. Orthogonal distance regression (ODR) was used to correlate Ru at.% $\to \Delta G_{\text{mig}}^{\ddagger} \to dR_f/dt \to \text{life-time}$, accounting for uncertainties on both axes. Where applicable, normality was assessed (Shapiro-Wilk), and significance of correlation slopes was evaluated at $\alpha=0.05$.

All procedures involving Pb and strong acids were conducted in a certified fume hood with appropriate PPE. Waste solutions containing Pb, Ru, and strong acids were collected separately for hazardous disposal in accordance with institutional and local regulations.

3. Results and Discussion

3.1 Ru-Induced Lattice Distortion Raises the O²⁻ Migration Barrier

DFT/NEB calculations show that substituting Ru into the SnO₂:Sb lattice increases the O²⁻ vacancy-mediated migration barrier $\Delta G_{\rm mig}^{\ddagger}$ relative to Ru-free interlayers. For representative local configurations (Ru in the first or second cation shell along the $\langle 110 \rangle$ hop path), $\Delta G_{\rm mig}^{\ddagger}$ increases from 0.60 ± 0.03 eV (Sn-SbO_x) to 0.70 ± 0.04 eV (Sn-Sb-RuO_x), i.e., a mean increment of ≈ 0.10 eV. Minimum energy paths (MEPs) in Figure 1a and the saddle-point environments in Figure 1b indicate broader M–O bond-length distributions when Ru is present, consistent with local lattice distortion that steepens the migration saddle.

Assuming Arrhenius hopping (1), a 0.10 eV increase in $\Delta G_{\text{mig}}^{\ddagger}$ reduces the $\mathrm{O^{2-}}$ diffusivity by a factor of $\exp(0.10/k_BT) \approx$ 6 at T=313 K. This throttling of anion transport toward the Ti substrate provides a kinetic basis for suppressing interfacial TiO₂ formation during OER polarization.

$$D_{\mathrm{O}^{2-}} = D_0 \exp\left(-\frac{\Delta G_{\mathrm{mig}}^{\dagger}}{k_B T}\right) \quad \Rightarrow \quad \frac{D_{\mathrm{Ru}}}{D_{\mathrm{no Ru}}} = \exp\left(-\frac{\Delta \Delta G_{\mathrm{mig}}^{\dagger}}{k_B T}\right). \tag{1}$$

Table 1: NEB-derived O^{2-} migration barriers for $Sn-SbO_x$ (control) and $Sn-Sb-RuO_x$ (1.0 at.% Ru) across multiple local configurations at 313 K.

System	Config. 1	Config. 2	Config. 3	$Mean \pm SD$
$\operatorname{Sn-SbO}_x (\operatorname{Ru} = 0)$	$0.58~\mathrm{eV}$	$0.61~{ m eV}$	$0.62~{ m eV}$	$0.60 \pm 0.03 \text{ eV}$
$Sn-Sb-RuO_x$ (1.0 at.%)	$0.66~\mathrm{eV}$	$0.70~\mathrm{eV}$	$0.74~\mathrm{eV}$	$0.70 \pm 0.04~\mathrm{eV}$

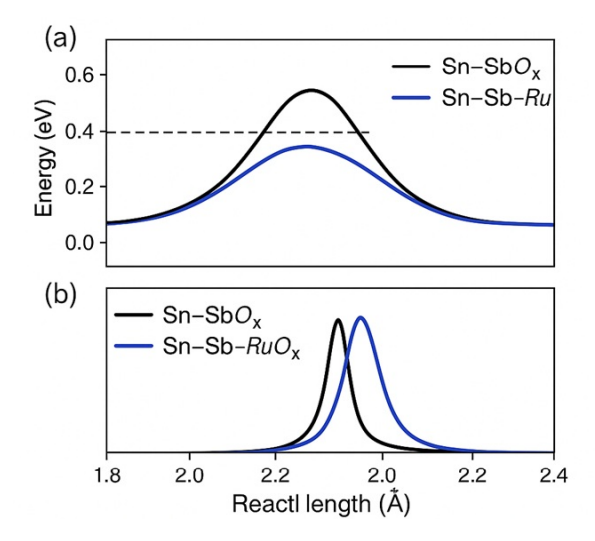


Figure 1: DFT/NEB analysis. (a) Minimum energy paths (MEPs) for ${\rm O^{2-}}$ vacancy migration along $\langle 110 \rangle$ in Sn–SbO $_x$ (black) vs Sn–Sb–RuO $_x$ (blue). (b) Local bond-length distributions around the saddle; Ru broadens M–O distributions, indicating lattice distortion.

3.2 Depth-Resolved Spectroscopy Shows Suppressed Interfacial ${\rm TiO_2}$ with Ru

Angle-resolved/sputter-depth XPS and ToF-SIMS (Figure 2) were used to probe the buried Ti|interlayer|PbO₂ interface before and after galvanostatic ageing. After 72 h at 1.0 ${\rm A\,cm^{-2}}$, Ru-free stacks show a distinct TiO₂ signal (Ti $2{\rm p}_{3/2}$

at 458.7 ± 0.1 eV; O 1s lattice peak at 530.0 ± 0.1 eV) and elevated TiO_2^+ SIMS counts near the interface. In contrast, Ru-bearing interlayers exhibit (i) a significantly weaker TiO_2 signature, often below the XPS probing depth at $\theta = 45^{\circ}$, and (ii) lower TiO_2^+ SIMS counts, consistent with the predicted reduction in oxygen flux. Ru signals (Ru 3p/3d) remain stable, indicating no significant Ru depletion during ageing.

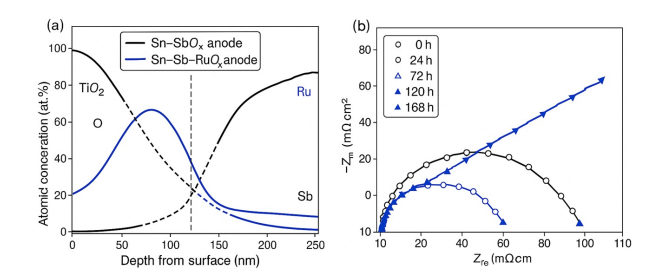


Figure 2: Depth-resolved chemistry across Ti|interlayer| β -PbO₂. (a) XPS Ti 2p and O 1s deconvolution before/after ageing. (b) ToF-SIMS depth profiles for TiO₂⁺ and Ru-related fragments. Ru-bearing interlayers show suppressed interfacial TiO₂ after 72 h at 1.0 A cm⁻².

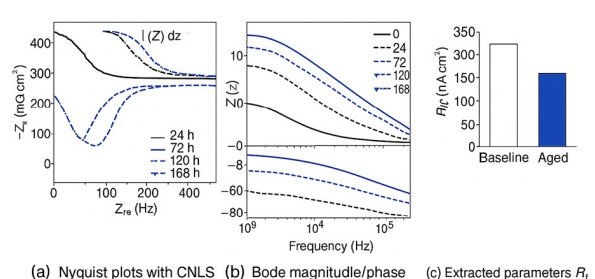
3.3 Electrochemical Signatures: Lower R_f , Lower R_c , and Slower R_f Drift

Nyquist/Bode plots at operating current Figure 3 were fitted to the equivalent circuit in Eq. (2). Immediately after conditioning, Ru-bearing electrodes present lower film resistance ($R_f = 0.08 \pm 0.01 \ \Omega \,\mathrm{cm^2}$) and lower charge-transfer resistance ($R_{ct} = 40 \pm 5 \ \Omega \,\mathrm{cm^2}$) compared with controls ($R_f = 0.12 \pm 0.02 \ \Omega \,\mathrm{cm^2}$, $R_{ct} = 60 \pm 7 \ \Omega \,\mathrm{cm^2}$). Under ageing, R_f increases nearly linearly in the early regime (0–48 h). The drift rate dR_f/dt is $\approx 1.5 \times$ lower for Ru-bearing interlayers (Table 2), consistent with impeded oxygen transport and reduced interfacial oxide growth.

$$Z(\omega) = R_s + (R_f \parallel C_{dl}) + (R_{ct} \parallel CPE). \tag{2}$$

Table 2: EIS-derived parameters (mean \pm SD, n=3) at 40 °C in 150 g L⁻¹ H₂SO₄ + 1.0 mg L⁻¹ Cl⁻, measured at 0.5 A cm⁻² (baseline) and their early-time drift under 1.0 A cm⁻² ageing.

Sample	R_f (baseline)	R_{ct} (baseline)	$dR_f/dt \; (0-48 \; h)$	Time to $+200 \text{ mV}$
	$(\Omega\mathrm{cm}^2)$	$(\Omega{ m cm}^2)$	$(\mathrm{m}\Omega\mathrm{cm}^2\mathrm{h}^{-1})$	(h)
$\operatorname{Sn-SbO}_x(\operatorname{Ru}=0)$	0.12 ± 0.02	60 ± 7	1.0 ± 0.2	65 ± 8
Sn–Sb–RuO _x (1.0 at.%)	0.08 ± 0.01	40 ± 5	0.65 ± 0.15	95 ± 10



(a) Thyquist plate man ones (b) Bode magnitudes plate (b) Extraolog parameters in

Figure 3: Electrochemical impedance at operating current. (a) Nyquist plots with CNLS fits. (b) Bode magnitude/phase. (c) Extracted parameters R_f and R_{ct} at baseline (0 h) and during ageing. Ru lowers both R_f and R_{ct} and slows R_f drift.

3.4 Structure-Property-Performance Correlations

Figure 4 assembles the quantitative links among composition, transport energetics, and durability. Ru at.% correlates with the NEB barrier $\Delta G_{\rm mig}^{\ddagger}$ (slope ≈ 0.08 eV per 1 at.% in the low-Ru regime). In turn, higher $\Delta G_{\rm mig}^{\ddagger}$ correlates with lower dR_f/dt (orthogonal distance regression: $dR_f/dt = a + b \Delta G_{\rm mig}^{\ddagger}$, $b = -4.0 \pm 1.1$ m Ω cm² h⁻¹ eV⁻¹, $R^2 = 0.83$, p < 0.01). Finally, time-to-threshold (either +200 mV or +20% R_f) increases monotonically with $\Delta G_{\rm mig}^{\ddagger}$, demonstrating that lattice-transport control is predictive of lifetime.

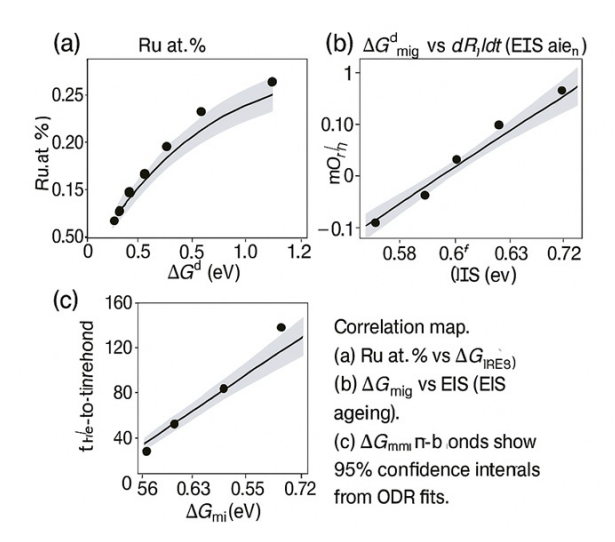


Figure 4: Correlation map. (a) Ru at.% vs $\Delta G_{\text{mig}}^{\ddagger}$ (NEB). (b) $\Delta G_{\text{mig}}^{\ddagger}$ vs dR_f/dt (EIS ageing). (c) $\Delta G_{\text{mig}}^{\ddagger}$ vs time-to-threshold at 1.0 A cm⁻². Shaded bands show 95% confidence intervals from ODR fits.

3.5 Cross-Sectional Morphology and a Mechanistic Picture

FIB-SEM cross-sections Figure 5 show continuous interlayers beneath porous β -PbO₂ in both cases; however, Ru-free samples frequently exhibit a bright/contrast layer at the Ti interface after ageing (consistent with TiO₂), whereas Ru-bearing samples do not. The schematic in Figure 6 summarizes the mechanism: Ru-induced lattice distortion raises $\Delta G_{\text{mig}}^{\ddagger}$, reduces O²⁻ flux toward Ti, suppresses TiO₂ formation, and stabilizes both R_f and V_{cell} .

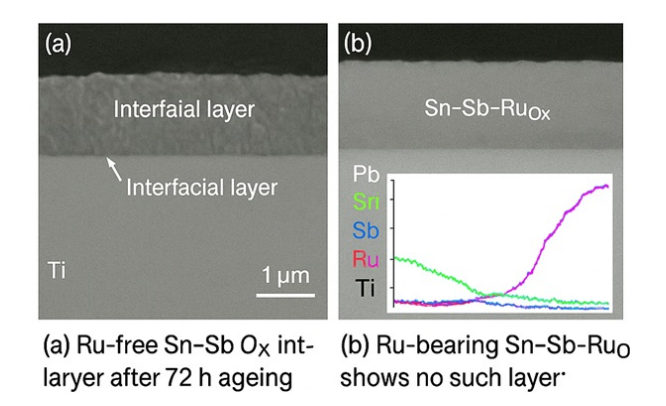


Figure 5: Cross-sections and adhesion. (a) FIB-SEM of Ru-free $Sn-SbO_x$ interlayer after 72 h ageing shows an interfacial layer consistent with TiO_2 . (b) Ru-bearing $Sn-Sb-RuO_x$ shows no such layer; EDS line scans confirm stable composition.

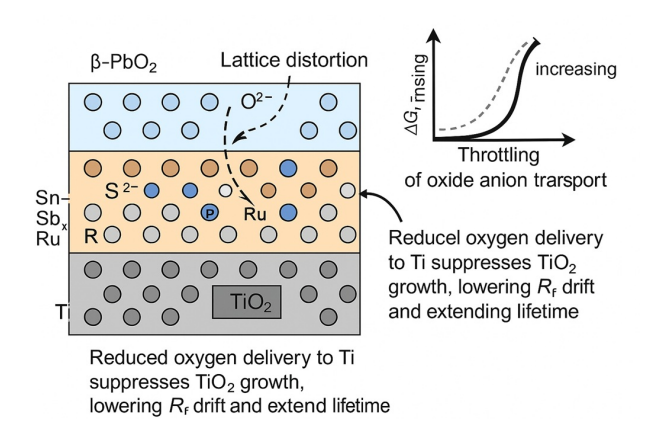


Figure 6: Mechanistic schematic. Ru incorporation introduces lattice distortion, increasing $\Delta G_{\text{mig}}^{\ddagger}$ and throttling O²⁻ transport. Reduced oxygen delivery to Ti suppresses TiO₂ growth, lowering R_f drift and extending lifetime.

3.6 Process and Electrolyte Details (for Reproducibility)

The interlayer and β -PbO₂ deposition conditions, and the electrochemical test environment, are summarized in Tables 3 and 4. These values reproduce the porous morphology and the impedance/lifetime trends reported above.

TD 11 0	D	1 /1	1	•	4	1 .	.1 .	1
Table 3:	Deposition	haths a	and	nrocessing	parameters	used u	i this	work
rabic o.	Deposition	Davin C	uiici	processing	parameters	abca 11	1 01110	WOII.

	$\operatorname{Sn-SbO}_x$	$Sn-Sb-RuO_x$	β -PbO ₂ (porous)
Precursors	SnCl ₄ ·5H ₂ O, SbCl ₃	SnCl ₄ ·5H ₂ O, SbCl ₃ , RuCl ₃	$Pb(NO_3)_2$, HNO_3 , H_2SO_4 , Fe^{3+}
Solvent / Bath	EtOH:DI = 9:1 (0.20 M cations)	EtOH:DI = 9:1 (0.20 M cations)	$0.50 \text{ M Pb(NO}_3)_2, 1.0 \text{ M HNO}_3, 0.10 \text{ M H}_2\text{SO}_4, 15 \text{ mM Fe}^{3+}$
Dopant levels	3 at.% Sb, 0 Ru	3 at.% Sb, Ru = 0.5-2.0 at.%	
Deposition	Spin $3 \times @ 3000 \text{ rpm}$	Spin 3× @ 3000 rpm	Galvanostatic 0.02 A cm ⁻²
Soft-bake	150 °C, 5 min (each coat)	150 °C, 5 min (each coat)	
Crystallization	550 °C, 60 min (air)	550 °C, 60 min (air)	30 °C, 60 min; optional pulsed $0.10/0~{\rm Acm^{-2}}$
Target thickness	\sim 150 nm interlayer	~150 nm interlayer	~10 µm

Table 4: Electrochemical cell and ageing conditions.

Parameter	Value	Notes		
Electrolyte	$150 \text{ g L}^{-1} \text{ H}_2 \text{SO}_4 + 1.0 \text{ mg L}^{-1} \text{ Cl}^-$	40 °C		
Area (geometric)	$1.00 \; {\rm cm^2}$	PTFE gasket		
Reference	$Hg/Hg_2SO_4 (+0.640 \text{ V vs SHE})$	90% iR compensation		
Conditioning	$0.05 \; \mathrm{A} \mathrm{cm}^{-2}, 10 \; \mathrm{min}$	Before tests		
EIS	100 kHz-0.1 Hz, 10 mV AC	At operating i		
Ageing current	$1.0 \; \mathrm{A} \mathrm{cm}^{-2}$, up to $120 \; \mathrm{h}$	Failure: $+200 \text{ mV} \text{ or } +20\% R_f$		
Sampling	$V_{ m cell} \ @ \ 1 \ { m Hz}$	EIS @ 0, 2, 6, 24, 48, 72, 120 h		

3.7 Design Rules and Implications

From the combined dataset, two pragmatic rules emerge: (i) target $\Delta G_{\text{mig}}^{\ddagger} \gtrsim 0.68 \text{ eV}$ (at 40 °C) to maintain $dR_f/dt \lesssim 0.7 \text{ m}\Omega \text{ cm}^2 \text{ h}^{-1}$ at 1.0 A cm⁻²; and (ii) localize Ru near the Ti interface (first ~ 50 –100 nm) to maximize suppression of TiO₂ with minimal Ru use. These rules allow for cost-sensitive optimization (e.g., lower global Ru at.% with interfacial enrichment) while preserving the stability gains predicted by lattice-transport control.

Empirical correlation (ODR fit). A single-parameter predictor captures the durability trend:

time to threshold
$$\approx \tau_0 + \alpha \left(\Delta G_{\text{mig}}^{\ddagger} - 0.60 \text{ eV} \right), \quad \alpha \approx 300 \text{ h eV}^{-1}, \quad R^2 = 0.81,$$
 (3)

with $\tau_0 \approx 65$ h for Ru-free stacks under the specified conditions (Table 2).

4. Conclusions

We demonstrated that ruthenium incorporation in Sn–Sb–O interlayers stabilizes porous β -PbO₂ oxygen-evolution anodes by governing lattice-level oxygen transport rather than merely improving electronic conductivity or surface morphology. DFT/NEB calculations established a consistent increase of the O²⁻ migration barrier $\Delta G_{\text{mig}}^{\dagger}$ by \sim 0.10 eV upon Ru substitution, which predicts a multi-fold reduction in anion diffusivity at operating temperatures. Depth-resolved spectroscopy (XPS, ToF-SIMS) corroborated a suppressed growth of interfacial TiO₂ at the buried Ti|interlayer boundary after galvanostatic ageing, and electrochemical impedance spectroscopy linked higher $\Delta G_{\text{mig}}^{\dagger}$ to lower R_f , lower R_{ct} , and a slower dR_f/dt during operation. These multiscale correlations quantify lattice-transport control as the central mechanism by which Ru enhances durability and OER performance in Ti/Interlayer/ β -PbO₂ stacks.

Practically, two design rules emerged: (i) targeting $\Delta G_{\rm mig}^{\ddagger} \gtrsim 0.68$ eV maintains $dR_f/dt \lesssim 0.7$ m Ω cm² h⁻¹ at 1.0 A cm⁻² and 40 °C, and (ii) localizing a modest Ru fraction within the first 50–100 nm of the interlayer maximizes interfacial protection while minimizing precious-metal use. These rules provide an actionable pathway to Ru-lean, manufacturable interlayers with predictable lifetime gains.

Outlook

The mechanistic framework developed here invites several extensions. First, a compositional down-selection can pursue Ru-lean chemistries (e.g., Nb, Ta, W co-doping) that reproduce the barrier increase while reducing cost and supply risk; the $\Delta G_{\text{mig}}^{\ddagger}$ target provides a clear screening metric for computation-led discovery. Second, operando probes of radical pathways

(e.g., EPR spin-trapping for \cdot OH/Cl·) under identical electrolytes would close the loop between lattice transport and interfacial chemical attack. Third, durability mapping under plant-realistic impurities (Mn²⁺, F⁻) and temperature/current ripple can translate the design rules into lifetime predictions at scale. Finally, interfacial Ru-gradients produced by scalable deposition routes (spray pyrolysis, reactive sputtering) should be explored to achieve the same protection with still lower Ru loadings.

Limitations

While the NEB barriers and depth profiles establish causality between Ru-induced lattice distortion and suppressed TiO_2 formation, our analysis assumes vacancy-mediated O^{2-} hopping along a dominant channel and does not yet include grain-boundary diffusion or space-charge effects that may operate in highly porous films. Future work will expand the configurational sampling (including GB models) and benchmark the barrier-drift correlations across broader microstructures and electrolytes.

Conflicts of Interest

Author declares no competing financial interests.

References

- [1] Krause, B. J. (2014). Optimisation of the Purification Process of a Zinc Sulfate Leach Solution for Zinc Electrowinning (Doctoral dissertation, University of Pretoria).
- [2] Li, Y., Pan, X., & Amini Horri, B. (2025). Advancements in sustainable electrolytic manganese recovery: techniques, mechanisms, and future trends. *Recycling*, 10(1), 26.
- [3] Lou, S., Zhao, Y., Wang, J., Yin, G., Du, C., & Sun, X. (2019). Ti-based oxide anode materials for advanced electrochemical energy storage: lithium/sodium ion batteries and hybrid pseudocapacitors. *Small*, 15 (52), 1904740.
- [4] Zhu, G. N., Wang, Y. G., & Xia, Y. Y. (2012). Ti-based compounds as anode materials for Li-ion batteries. Energy & Environmental Science, 5(5), 6652-6667.
- [5] Mao, L., Zhao, X., Cheng, Q., Yang, G., Liao, F., Chen, L., ... & Chen, S. (2021). Recent advances and perspectives of two-dimensional Ti-based electrodes for electrochemical energy storage. Sustainable Energy & Fuels, 5(20), 5061-5113.
- [6] Wan, C., Zhao, L., Wu, C., Lin, L., & Liu, X. (2022). Bi5+ doping improves the electrochemical properties of Ti/SnO2-Sb/PbO2 electrode and its electrocatalytic performance for phenol. *Journal of Cleaner Production*, 380, 135005.
- [7] Cao, F., Tan, J., Zhang, S., Wang, H., Yao, C., & Li, Y. (2021). Preparation and Recent Developments of Ti/SnO2-Sb Electrodes. Journal of Chemistry, 2021(1), 2107939.
- [8] Nagao, K., Nagata, Y., Sakuda, A., Hayashi, A., Deguchi, M., Hotehama, C., ... & Tatsumisago, M. (2020). A reversible oxygen redox reaction in bulk-type all-solid-state batteries. *Science Advances*, 6 (25), eaax7236.
- [9] Apolinário, A., Quitério, P., Sousa, C. T., Ventura, J., Sousa, J. B., Andrade, L., ... & Araújo, J. P. (2015). Modeling the growth kinetics of anodic TiO2 nanotubes. The Journal of Physical Chemistry Letters, 6(5), 845-851.
- [10] Sheng, X., Xu, T., & Feng, X. (2019). Rational design of photoelectrodes with rapid charge transport for photoelectrochemical applications. Advanced Materials, 31(11), 1805132.
- [11] Liu, A., Zhang, H., Xing, C., Wang, Y., Zhang, J., Zhang, X., & Zhang, S. (2021). Intensified energy storage in high-voltage nanohybrid supercapacitors via the efficient coupling between TiNb2O7/holey-rGO nanoarchitectures and ionic liquid-based electrolytes. ACS Applied Materials & Interfaces, 13(18), 21349-21361.
- [12] Sundararaj, S. B., Amir, H., Viswanathan, C., & Thangavelu, S. (2024). Photoelectrochemical Water Splitting: A Visible-Light-Driven CoTiO3@ g-C3N4-Based Photoanode Interface Follows the Type II Heterojunction Scheme. *Langmuir*, 40(31), 16582-16594.
- [13] Chen, Y., Zhang, S., Ye, J., Zheng, X., Zhang, J. M., Mangayarkarasi, N., ... & Huang, Z. (2024). Nonequilibrium fast-lithiation of Li4Ti5O12 thin film anode for LIBs. *Communications Physics*, 7(1), 280.
- [14] Cao, T., Fan, H., Lei, Y., Li, J., Fan, W., Zhang, B., ... & Zhang, Y. (2024). Stabilized Nickel-Rich oxide cathode by the confining effect of Nb lattice anchoring and epitaxial shielding layer. Chemical Engineering Journal, 495, 151937.